October 2008
SLAC-PUB-13449

Chemical Bonding, Interfaces and Defects in Hafnium Oxide/Germanium Oxynitride Gate Stacks on Ge (100)

Yasuhiro Oshima[*,*4], Yun Sun[**], Duygu Kuzum[***], Takuya Sugawara[*4], Krishna C. Saraswat[***], Piero Pianetta[**], and Paul C. McIntyre[*]

[*]Department of Materials Science and Engineering, Stanford University, Stanford, CA 94305, USA
[**]Stanford Synchrotron Radiation Laboratory, Stanford, CA 94305, USA
[***]Department of Electrical Engineering, Stanford University, Stanford, CA 94305, USA
[*4]Tokyo Electron U. S. Holdings, Inc., Santa Clara, CA 95054, USA

Published in the Journal of Electrochemical Society

Work supported in part by US Department of Energy contract DE-AC02-76SF00515

Abstract

Correlations among interface properties and chemical bonding characteristics in $HfO_2/GeO_xN_y/Ge$ MIS stacks were investigated using *in-situ* remote nitridation of the Ge (100) surface prior to HfO_2 atomic layer deposition (ALD). Ultra thin (~1.1 nm), thermally stable and aqueous etch-resistant GeO_xN_y interfaces layers that exhibited Ge core level photoelectron spectra (PES) similar to stoichiometric Ge_3N_4 were synthesized. To evaluate GeO_xN_y/Ge interface defects, the density of interface states (D_{it}) was extracted by the conductance method across the band gap. Forming gas annealed (FGA) samples exhibited substantially lower D_{it} (~$1x10^{12}$ $cm^{-2}eV^{-1}$) than did high vacuum annealed (HVA) and inert gas anneal (IGA) samples (~$1x10^{13}$ $cm^{-2}eV^{-1}$). Germanium core level photoelectron spectra from similar FGA-treated samples detected out-diffusion of germanium oxide to the HfO_2 film surface and apparent modification of chemical bonding at the GeO_xN_y/Ge interface, which is related to the reduced D_{it}.

Germanium is an attractive material for high performance metal oxide semiconductor field effect transistor (MOSFET) channels because of its high hole and electron mobilities[1]. However, compared to the SiO_2/Si system, Ge oxides grown on Ge semiconductor have undesirable physical and electrical properties for field effect devices. Their poor thermal stability, solubility in water and tendency for nonstoichiometry make it difficult to utilize germanium oxides as an interface layer interposed between high-k dielectrics and the Ge substrate surface in a practical MOSFET fabrication process. Engineering a stable interface layer between the high-k film and Ge is vital to achieving dimensionally-scaled, high speed, field effect transistors. Previous studies on high-k/Ge gate stacks with interfacial layers such as germanium nitride and oxynitride have been reported[2, 3, 4, 5]. However, the relationships among electrical properties, and the binding states of Ge in the interface and thermal stability of the gate stacks are not yet well understood.

Maeda et al[3]. and Otani et al[4]. obtained low D_{it} (1.8×10^{11}, 4×10^{11} $cm^{-2}eV^{-1}$) with HfO_2 and Ta_2O_5 on the top of relatively thick Ge_3N_4 layers (~2 nm), respectively. They reported that Ge_3N_4 layers were not oxidized during high-k metal oxide deposition, and that an interface between Ge_3N_4 and Ge with reasonably low defect density was achieved. However, considering the technology node in which Ge technology may be applied, the interface layer between channel and high-k film should be substantially thinner than 2 nm in order to allow scaling of the gate capacitance density. Moreover, interface layers must exhibit resistance to oxidation during post-deposition thermal processes. Therefore, in the present work, we focus on the MOS interface properties and their relationship to chemical bonding of Ge in the gate stack.

Experimental

(100) Sb-doped n-type Ge wafers with 0.04-0.047 Ω cm (Umicore) were cleaned in 50:1 HF solution followed by deionized water rinse (5 cycles) and dried in high purity N_2. Wafers were loaded into a load-locked ALD system with ICP remote plasma source immediately after wet cleaning to avoid Ge surface oxidation. A detailed schematic diagram of the ALD system has been reported elsewhere[6]. Radical nitridation using a remote inductively coupled plasma (ICP) source (Advanced Energy Inc., LB1501) followed by HfO_2 deposition using tetrakisdiethylamino hafnium (TDEAH, from Praxair) precursor and water vapor oxidant were performed to prepare HfO_2/GeO_xN_y gate stacks. For surface and interface characterization, x-ray photoelectron spectroscopy (XPS, S-Probe, Surface Science Instruments), synchrotron radiation photoelectron spectroscopy (SRPES, Stanford Synchrotron Radiation Laboratory beam line 10-1) with a PHI (model 10-360) hemispherical energy analyzer and multichannel detector. Pt electrodes were deposited by electron beam evaporation through a metal shadow mask to measure capacitance-voltage, conductance-voltage and current-voltage characteristics. The electrodes were circular with diameters of either 100 μm or 150 μm.

Result and Discussion

The optimized *in-situ* nitridation process for the Ge (100) surface used active species generated in a remote plasma composed of a $H_2/N_2/Ar$ gas mixture, with a substrate temperature of 435°C. Systematic comparisons of aqueous etching rates of GeO_xN_y films fabricated with N_2/Ar (A), $H_2/N_2/Ar$ (B) and $H_2/N_2/NH_3/Ar$ (C) gas mixtures were carried out to investigate optimal plasma composition for nitridation. Figure 1 shows Ge 3d core level XPS spectra using conventional Al Kα (1486.6 eV) radiation before and after deionized water etching for 120 sec. The dotted lines indicate the peak position for GeO (+1.4 eV shift versus Ge^0), Ge_3N_4 (+2.0 eV),

GeO_2 (+3.2 eV), as reported in the literature[7, 8]. In the case of N_2/Ar plasma ambient, a dominant oxynitride component was observed in with Ge 3d core level chemical shift between those expected for pure Ge_3N_4 and GeO_2, (a shift of +2.2 eV relative to Ge^0). The N 1s spectra shows that the N_2/Ar sample has a larger binding energy shift (~0.4 eV) than the other two plasma chemistries, suggestive of oxidation of the nitride layer to form $–NO_x$ species in the oxynitride layer. Moreover, a dramatic decrease in peak intensity was observed after aqueous etching of this oxynitride. In the case of H_2/N_2/Ar plasma, Ge oxynitride components could be deconvoluted reasonably using the literature values of core level chemical shifts described above. Comparing these two conditions, the 3d germanium oxide feature intensity decreased less in the H_2/N_2/Ar case after aqueous etching. This decrease is attributed to dissolution of a thin GeO_2 layer on the top surface of the GeO_xN_y. This layer likely forms during air exposure after plasma nitridation and prior to XPS measurement. Before and after aqueous etching, nitrogen to germanium component ratios (N/Ge) were 0.94 and 1.35 respectively, indicating that the nitride formed by remote plasma nitridation at elevated substrate temperatures is similar to stoichiometric Ge_3N_4 (N/Ge = 1.33).

These results may indicate the formation of Ge-NH-Ge or Ge-N bonds in the oxynitride layer, rather than incorporation of amine ($-NH_x$) or nitroxyl ($-NO_x$) groups. Mui's first principle calculation[9] shows that Ge-NH-Ge formation for Ge is slower and less thermodynamically favorable than the equivalent process for Si. In the case of $NH_3/N_2/H_2$/Ar samples, species such as NH_x, which are easily oxidized, may be formed predominantly due to the higher concentration of H species than for the N_2/H_2/Ar chemistry. On the other hand, in the case of N_2/Ar, the absence of hydrogen in the plasma seems to alter the structure of the film so that it becomes more readily oxidizable. In the latter case, we observed large voltage hysteresis in CV curves

obtained from the corresponding Pt/GeO_xN_y/Ge MOS capacitors (data not shown), indicating the presence of a large density of electron traps in the gate stack. These results indicate that careful control of the N/H ratio is required for stable Ge-N bond formation using remote ICP nitridation. Therefore, H_2/N_2/Ar plasma was typically used for interfacial layer formation in the experiments reported herein.

The thickness of the GeO_xN_y layer d (Figure 1, (b)) was estimated using the following calculation procedure reported by Carlson and McGuire[10].

$$\frac{I_{GeON}}{I_{Ge}} = \frac{\sigma_{GeON} N_{GeON} \lambda_{GeON} (1 - \exp A)}{\sigma_{Ge} N_{Ge} \lambda_{Ge} \exp A}$$

$$A = \frac{-d}{\lambda_{GeON} \sin \theta}$$

where I_{GeON} and I_{Ge} are the intensities of Ge 3d core level photoelectrons detected from the GeO_xN_y layer and Ge substrate, σ_{GeON} and σ_{Ge} are the photoelectron cross sections, N_{GeON} and N_{Ge} are the surface atomic densities of Ge in each layer, λ_{GeON} and λ_{Ge} are the mean-free paths of electrons, and θ (35^o in this study) is the angle of the detector relative to the sample surface. We assumed λ_{GeON} to be equal to λ_{Ge} and λ_{Ge} ~ 2.8 nm (kinetic energy ~1450 eV), according to the calculation by Tanuma, Powell and Penn[11]. σ_{GeON} was also assumed to be equal to σ_{Ge}. The surface atomic density of Ge atoms in the GeO_xN_y layer was taken from reported simulation data of Ge_3N_4[12] (~3.4 x 10^{22} atoms cm^{-3}). By using these assumptions, we calculate a GeO_xN_y layer thickness of 1.1 nm.

Thermal stability of the GeO_xN_y film was also investigated by *in-situ* annealing in the XPS chamber using the N_2/H_2/Ar sample, as shown in Figure 2. The sample was loaded into the XPS chamber immediately after nitridation to prevent oxidation and heated step-wise pattern in the XPS chamber from 200 °C to 500 °C. The ratio of nitrogen to oxynitride components in Ge 3d spectrum (N/GeON) was calculated by the formula as shown below.

$$N/GeON = \frac{\frac{A_{N1s}}{S_{N1s}}}{\frac{A_{Ge3d}}{S_{Ge3d}} - \frac{A_{Ge^0}}{S_{Ge3d}}}$$

Where $A_{N\ 1s}$ and $A_{Ge\ 3d}$ are the XPS peak area of each elements, and A_{Ge}^0 is the peak area of Ge^0 component determined by peak fitting. $S_{N\ 1s}$ and $S_{Ge\ 3d}$ are the relative sensitivity factors of N 1s and Ge 3d core levels, respectively. The N/GeON ratio after in-situ anneals was almost constant for temperatures up to 500 °C, indicating that this GeO_xN_y film has sufficient thermal stability for typical dopant activation anneal temperatures in Ge devices[13]. Loss of oxygen from the sample can be attributed to desorption of oxygen-containing species including GeO(g)[12] in the air-exposed surface region of the oxynitride film.

After GeO_xN_y formation in the ALD reactor, HfO_2 was deposited at 150°C using TDEAH and H_2O precursors without breaking vacuum. The samples were taken out to atmosphere after cooling down under vacuum in the load lock chamber. The interface reaction between the overlying HfO_2 layer and GeO_xN_y was observed by SRPES which has significant advantages over conventional XPS, such as higher energy resolution and higher surface sensitivity due to its lower incident photon energy. Low energy photons are of particular interest in these experiments because the overlap between the Hf 5p peak and Ge 3d peaks is minimal at

an incident energy of ~200 eV due to the difference of each core level's cross section[14]. Figure 3 shows photoelectron spectra taken after *in-situ* anneal in the SRPES chamber. To observe the entire layer structure from Ge substrate to HfO_2 layer, a HfO_2 layer of ~1 nm thickness was deposited onto the GeO_xN_y interface layer. The binding energy of Ge 3d photoelectrons from GeO_xN_y components shifts to lower energies as the anneal temperature increases [Fig. 3(a)]. This is consistent with thermal decomposition of a thin GeO_2 layer that formed on the GeO_xN_y layer during the ALD process, forming volatile GeO[15]. The O 1s spectrum in Fig. 3(c) is also suggestive of decomposition of GeO_2 during the *in-situ* vacuum anneal in the SRPES chamber. A shoulder on the O 1s feature of the as-deposited sample (~531.5 eV) can be attributed to either a GeO_2 surface region on the air-exposed oxynitride layer or residual –OH groups incorporated in the ALD-HfO_2 film as a result of the use of the H_2O oxidant precursor during ALD[16]. Removal of oxygen from the interfacial GeO_xN_y layer is also consistent with the negative N 1s peak binding energy shift at higher temperature [Fig. 3(d)]. The peak shift of the Hf 4f feature during the anneal was small [Fig. 3(b)], indicating that any effect the anneal may have had on the oxidation state of Hf ions in the HfO_2 layer is beyond the experiment's detection limit.

As described subsequently, forming gas (H_2/Ar = 50/1000 sccm, 20 Torr) anneals (FGA), inert gas (Ar = 1000 sccm, 20 Torr, 30 min) anneals (IGA) and high vacuum anneals (HVA) were used as post-metallization anneals prior to electrical characterization of MIS capacitors on Ge. These anneals were done for 30 minutes. To probe the effects of these different anneals on chemical bonding in the HfO_2/GeO_xN_y stacks, samples with thick (~4 nm) and thin (~1 nm) HfO_2 were prepared. These samples make it possible to investigate diffusion of Ge and its oxides into the overlying HfO_2 layers and resulting changes in bonding states of the oxynitride interface layer. FGA and IGA were performed at 20 Torr and HVA was performed in the SRPES chamber

at ~2x10^{-9} Torr. Figure 4 compares core level spectra (Hf 4f, Ge 3d, O 1s, N 1s) of FGA (370 °C), HVA (500 °C) and as-deposited samples. An N 1s feature was not detected for the 4 nm HfO_2 samples due to the limited probing depth of SRPES; therefore, Figure 4 does not show N 1s spectra. The depth resolution of these measurements is indicated in the Ge 3d and N 1s spectra measured with 200 eV and 620 eV soft X-rays. Because the kinetic energies of Ge 3d photoelectrons are smaller than for the N 1s, their escape depth is also smaller. Therefore, in the case of Ge 3d, the depth beneath the surface from which signal can be collected is estimated as < 4 nm, and we can assume that the Ge 3d signal detected comes almost entirely from Ge diffused into overlying HfO_2 layer. To clarify the peak position and the contribution of Hf 5p peak, all the Ge 3d peak intensities are normalized by Hf 4f peak intensities. Without annealing, there is no Ge 3d feature detected, but the Hf 5p peak was observed at a binding energy of approximately 33 eV. After FGA and IGA, Ge 3d peaks which were shifted by + 2.8 eV from Ge^0 was detected. After HVA, the Ge 3d peak appears with a lower binding energy shift (~2.2 eV) than for the FGA sample. These binding energy shifts are considered to correspond to a mixture of Ge^{3+}(2.6 eV) and Ge^{4+}(3.2 eV) and a mixture of Ge^{2+}(1.8 eV) and Ge^{3+}(2.6 eV) oxidation states[17].

Figure 5(a) shows the Ge 3d spectrum for 1 nm thickness HfO_2 samples. Interestingly, the 1 nm FGA sample has a greater concentration of higher binding energy components corresponding to Ge^{4+} than does the IGA and HVA sample. Comparing with as-deposited spectrum, both IGA and HVA showed negative binding energy shifts. This suggests that the FGA may promote chemical changes leading to an increased Ge^{4+} oxidation state within the GeO_xN_y layer itself, not only on the HfO_2 surface as found for the corresponding 4 nm HfO_2 sample. As is the case for the 1 nm HfO_2 sample, the O 1s feature of the 4 nm HfO_2 sample [Figure 4(c)] had its higher binding energy shoulder removed after HVA. On the other hand,

after FGA, the photoelectron intensity at higher binding energies around GeO_2 feature decreased, but not by as much as after HVA. The significant high binding energy shoulder detected on the Ge 3d feature after FGA is attributed to Ge in the 4+ oxidation state, consistent with GeO_2. In the case of IGA, the intensity of higher binding energy feature of O 1s is slightly higher than for the FGA case. This higher energy feature is consistent with the presence of hydroxyl groups, therefore, this result may indicate that hydrogen annealing enhances OH removal from the gate stack. As evident in [Fig. 5(d)], the N 1s peak after FGA seems to correspond to a structure intermediate between the as-deposited and IGA, HVA samples. Comparison of full width at half maximum (FWHM) of the N 1s feature is also interesting. HVA and IGA decrease the FWHM (HVA = 1.38 eV, IGA = 1.38 eV) compared to the as-deposited sample (1.52). On the other hand, FGA increases the FWHM (to 1.75 eV). This indicates that FGA increases the range of chemical states of nitrogen in the GeO_xN_y perhaps because of a higher oxygen concentration introduced into the oxynitride, as expected from the higher binding energy shift of Ge 3d (Figure 5 (a)).

Comparison of the peak areas in Fig. 4(a) indicates that the areal density of Ge that diffuses into the 4 nm HfO_2 layer is greater in the FGA case than in the HVA or IGA case. This suggests that hydrogen annealing promotes GeO_2 segregation to the HfO_2 surface perhaps by increasing the effective diffusivity of Ge (oxide) across the HfO_2 layer. Secondary ion mass spectroscopy (SIMS) of these stacks was performed and the results confirmed a higher Ge concentration in the HfO_2 layer of FGA sample compared to HVA and as-deposited cases (not shown).

Platinum gate electrodes were deposited by electron beam evaporation through a shadow mask to make MIS capacitors. Figure 6 shows CV and IV characteristics of FGA, IGA and HVA (~2 x 10^{-6} Torr) sample. For electrical measurements, all the anneals were done at 370°C for 30

min after Pt deposition. Capacitance equivalent thicknesses of these samples were ~1.7 nm, calculated from CV curves in accumulation at 1 kHz. The CV curve of the FGA sample shows less frequency dispersion and a smaller shoulder in depletion, which suggests that FGA gives a lower density of interface states (D_{it}) than does HVA and IGA for these samples, although the FGA samples have a higher gate leakage current. The higher Ge concentration in the HfO_2 for the FGA sample may enhance the gate leakage current density by forming defects and lowering the Schottky barrier at the metal/insulator interface. However, the leakage conduction behavior of te IGA sample, which showed similar leakage current compared to FGA sample, despite the smaller concentration of Ge which was detected in HfO_2 layer.

Because Ge has higher carrier concentrations and a smaller band gap than does Si, the conductance behavior of high-k/Ge MOS capacitors is different from that of high-k/Si devices at room temperature[18, 19]. Figure 6 (c) shows the D_{it} distribution extracted by the conductance method[20] from 77 K to 250 K. At lower temperatures, the Fermi energy of the Ge substrate moves closer to the conduction band edge, as a result of the temperature dependence of the bandgap. This makes it possible to measure the D_{it} distribution in the upper half of the band gap over the typical frequency range of high-frequency CV measurements of capacitors formed on n-type Ge substrates. As-deposited, IGA and HVA samples exhibited an extracted $D_{it} > 10^{13}$ $cm^{-2}eV^{-1}$ near mid gap and HVA showed ~$1x10^{14}$ $cm^{-2}eV^{-1}$ near the conduction band edge. On the other hand, the D_{it} of the FGA sample was substantially lower (~$1x10^{12}$ $cm^{-2}eV^{-1}$) than for either the as-deposited or HVA samples. Both p- and n- type Ge substrates were used for the FGA samples to obtain the D_{it} distribution across the entire band gap.

Previous reports have suggested that a GeO_2-like interface layer has fewer defects than a suboxide-like Ge interface layer between deposited metal oxide gate insulators and the Ge (100)

channel[2,21]. Interface trap densities of ~6 x 10^{10} $cm^{-2}eV^{-1}$ and ~2 x 10^{11} $cm^{-2}eV^{-1}$ were repoted for Si_3N_4/GeO_2/p-Ge and Si_3N_4/GeO_xN_y/p-Ge gate stacks, respectively. The somewhat higher D_{it} observed for GeO_xN_y in the present experiments may be caused by the presence of nitrogen near the interface. We obtained relatively higher D_{it} values (~1 x 10^{12} $cm^{-2}eV^{-1}$) compared to previous reports[3, 4] even after FGA. Thinner interface layer thickness may cause a greater defect density by, for example, sub-oxide formation near the interface during the ALD process.

Recent theoretical results predict that hydrogen atoms should be ineffective passivants for interface states on Ge, unlike the case of SiO_2/Si[22] and this prediction is consistent other reported experimental results[23]. Therefore, the marked improvement in electrical characteristics observed in our samples after FGA annealing suggests that primary role of hydrogen annealing in the current experiments was to produce a more GeO_2-like environment at the GeO_xN_y/Ge interface and thus reduce D_{it}. This process appears to involve the removal of residual hydroxyl species from the ALD-HfO_2 film during hydrogen annealing and the simultaneous oxidation of the oxynitride layer which produces additional GeO_2-like bonding at the interface and diffusion of Ge-containing species toward the HfO_2 film surface.

Conclusions

To summarize, we have investigated the thermal stability of remote plasma-grown germanium oxide layers on Ge (100) in detail. High substrate-temperature nitridation conditions using a hydrogen and nitrogen-containing plasma produced an oxynitride layer that was resistant to aqueous etching and retained predominantly Ge_3N_4-like bonding during annealing to 500˚C. Effects of annealing HfO_2/GeO_xN_y/Ge gate stacks in forming gas and high vacuum conditions on

the chemical states of Ge were compared. Forming gas anneal was found to promote Ge oxide segregation to the HfO_2 surface and photoelectron binding energy shifts consistent with a greater Ge^{4+} component near the substrate interface. After post-metallization anneals with a Pt gate electrode present, it was found that the FGA samples exhibited lower D_{it} than comparable inert gas annealed, high vacuum annealed or as-deposited samples.

Acknowledgement

This work was supported by Stanford Initiative of Nanoscale Materials and Processes, and the MSD Focus Center Research Program. Portions of this research were carried out at Stanford Nanofabrication Facility and Stanford Synchrotron Radiation Laboratory. The authors also would like to acknowledge to Advanced Energy Industries, Inc. (for the remote plasma source) and Praxair, Inc. (for hafnium precursor).

Figure captions

Figure 1. Ge 3d XPS spectra of GeO_xN_y films which were nitrided under different gas conditions: (A) N_2/Ar, (B) H_2/N_2/Ar, (C) $H_2/N_2/NH_3$/Ar.

Figure 2. *In-situ* anneal temperature dependence of relative atomic ratio of nitrogen and oxygen to oxinitride components in GeO_xN_y film.

Figure 3. (a) Ge 3d, (b) Hf 4f, (c) O 1s and (d) N 1s core level SRPES spectra of a HfO_2 (~1 nm) /GeO_xN_y/n-Ge stack as a function of *in-situ* anneal temperature..

Figure 4. (a) Ge 3d, (b) Hf 4f, (c) O 1s and (d) N 1s core level SRPES spectra of HfO_2 (~4 nm) on GeO_xN_y/n-Ge stack after different post anneals. After forming gas anneal (FGA, open circle), inert gas (Ar) anneal (IGA, open square), high vacuum anneal (HVA, solid triangle) and as-deposited samples (straight line) are compared. Due to the thick over lying HfO2 film, N 1s in the GeO_xN_y layer was not detected for all the samples.

Figure 5. (a) Ge 3d, (b) Hf 4f, (c) O 1s and (d) N 1s core level SRPES spectra of HfO_2 (~1 nm) on GeO_xN_y/n-Ge stack after different post anneals. After forming gas anneal (FGA, open circle), inert gas (Ar) anneal (IGA, open square), high vacuum anneal (HVA, solid triangle) and as-deposited samples (straight line) are compared.

Figure 6. (a) CV (at 100 kHz) and (b) IV characteristics of Pt/HfO_2/GeO_xN_y/n-Ge MOS capacitor after different post-treatments and (c) interface states density distribution of band gap extracted by CV curves at low temperature (77-250 K) using conductance method.

Figure 1.

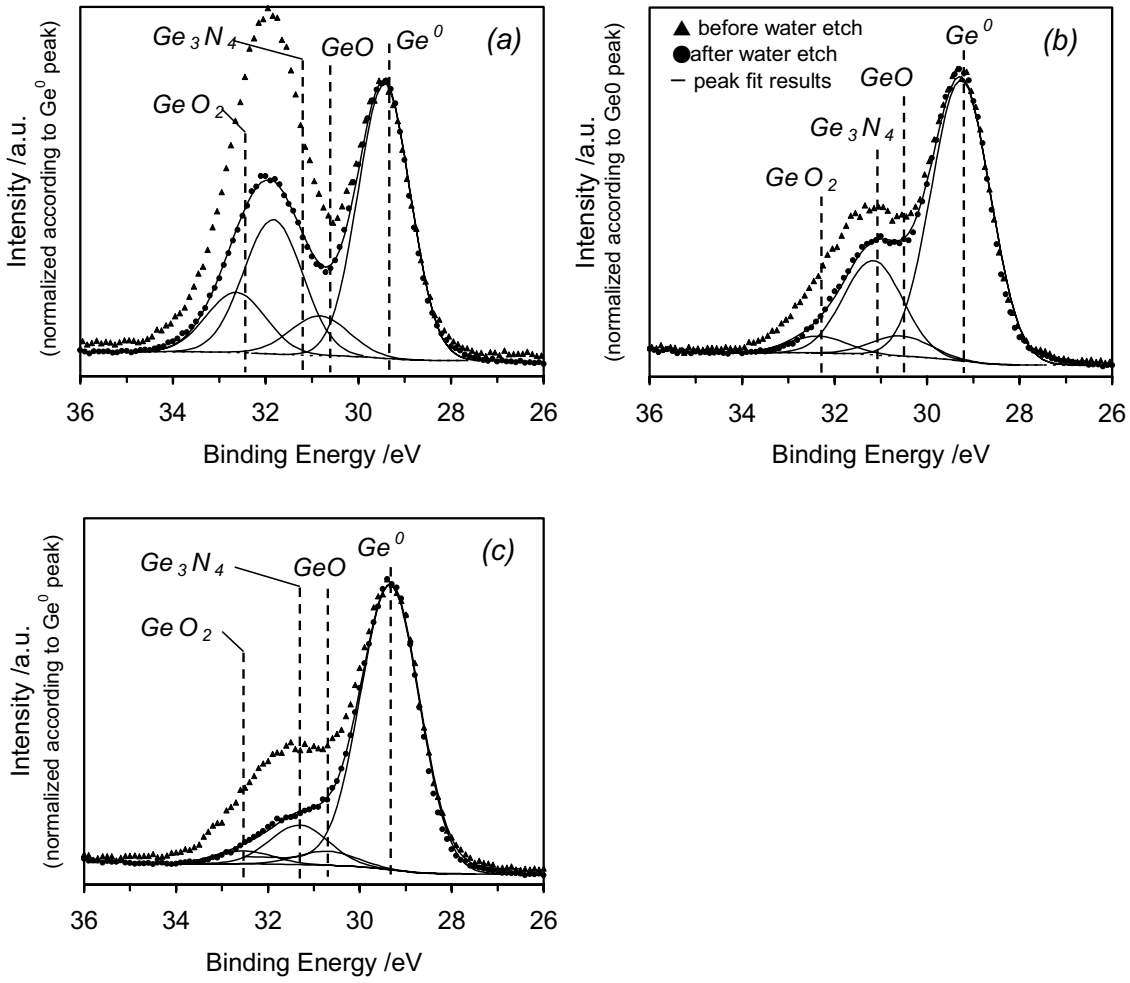
Ge 3 N 4
GeO
Ge 0
(a)
Ge O 2
Intensity /a.u.
(normalized according to Ge0 peak)
36
34
32
30
28
26
Binding Energy /eV
▲ before water etch
●after water etch
– peak fit results
(b)
(c)

Figure 2.

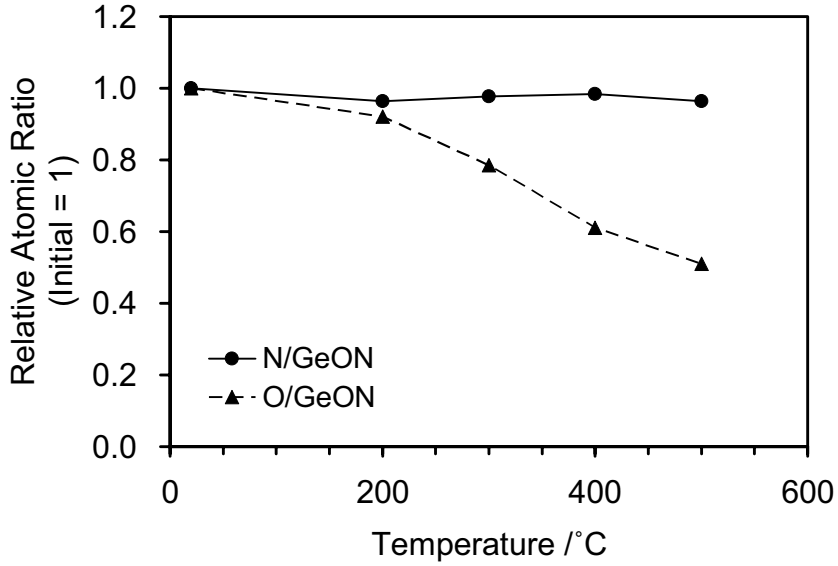
Relative Atomic Ratio
(Initial = 1)
1.2
1.0
0.8
0.6
0.4
0.2
0.0
0
200
400
600
Temperature /˚C
N/GeON
O/GeON

Figure 3.

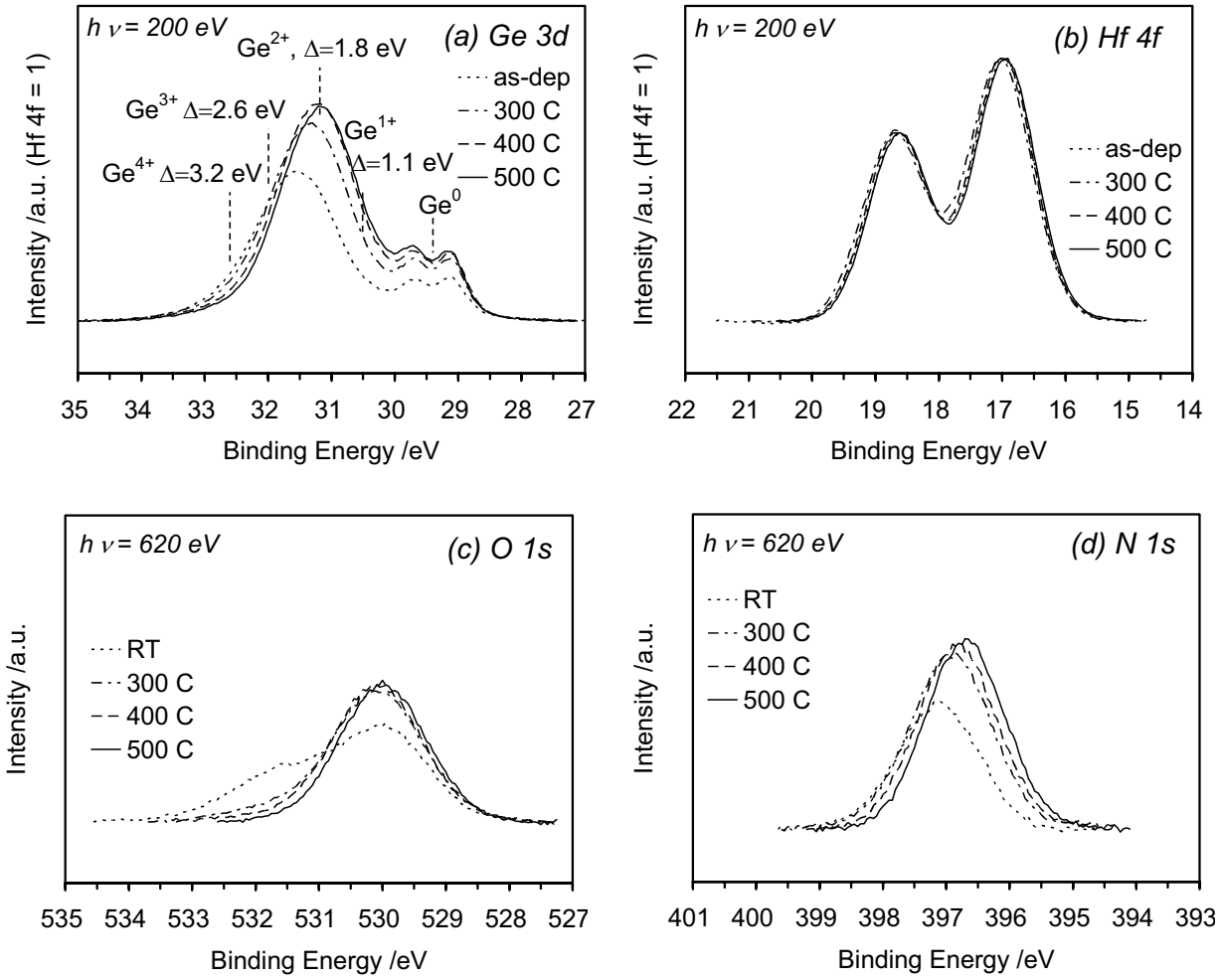
h ν = 200 eV
(a) Ge 3d
Ge2+, Δ=1.8 eV
Ge3+ Δ=2.6 eV
Ge1+ Δ=1.1 eV
Ge4+ Δ=3.2 eV
Ge0
as-dep
300 C
400 C
500 C
Intensity /a.u. (Hf 4f = 1)
Binding Energy /eV
h ν = 200 eV
(b) Hf 4f
as-dep
300 C
400 C
500 C
Intensity /a.u. (Hf 4f = 1)
Binding Energy /eV
h ν = 620 eV
(c) O 1s
RT
300 C
400 C
500 C
Intensity /a.u.
Binding Energy /eV
h ν = 620 eV
(d) N 1s
RT
300 C
400 C
500 C
Intensity /a.u.
Binding Energy /eV

Figure 4.

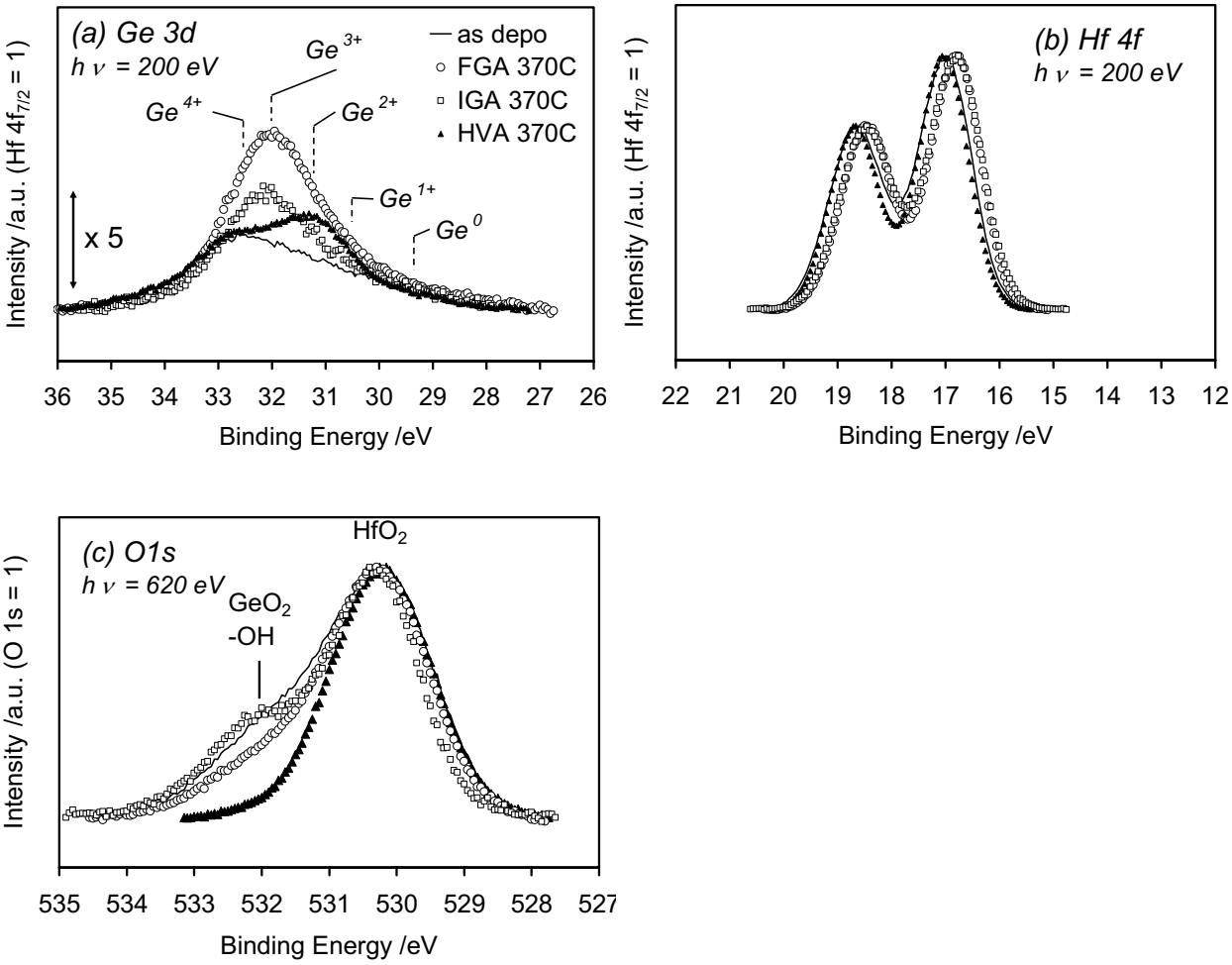
(a) Ge 3d
h ν = 200 eV
Ge 3+
Ge 4+
Ge 2+
Ge 1+
Ge 0
as depo
FGA 370C
IGA 370C
HVA 370C
x 5
Intensity /a.u. (Hf 4f7/2 = 1)
Binding Energy /eV
(b) Hf 4f
h ν = 200 eV
Intensity /a.u. (Hf 4f7/2 = 1)
Binding Energy /eV
(c) O1s
h ν = 620 eV
HfO2
GeO2
-OH
Intensity /a.u. (O 1s = 1)
Binding Energy /eV

Figure 5.

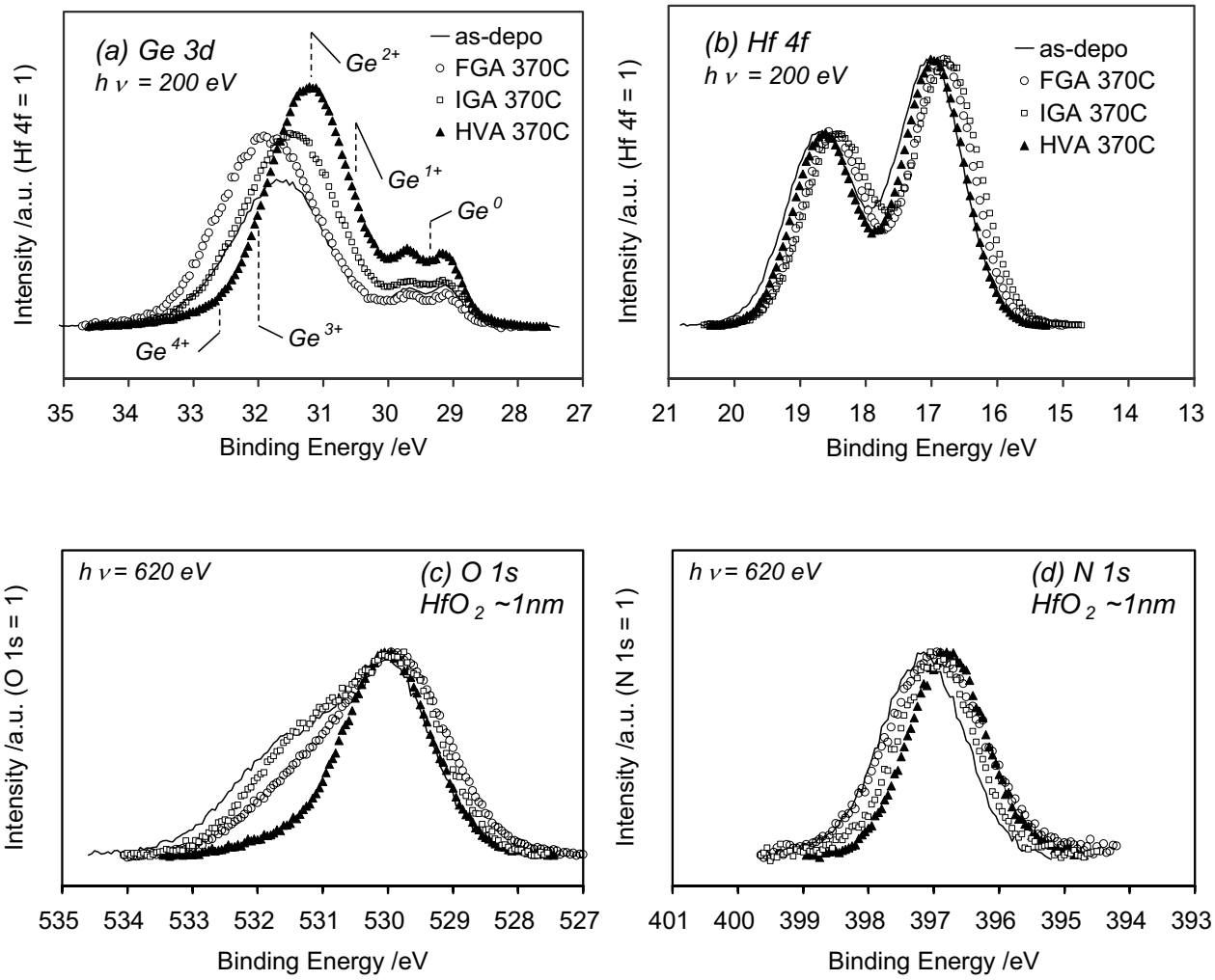
(a) Ge 3d
h ν = 200 eV
as-depo
FGA 370C
IGA 370C
HVA 370C
Ge 2+
Ge 1+
Ge 0
Ge 4+
Ge 3+
Intensity /a.u. (Hf 4f = 1)
Binding Energy /eV
(b) Hf 4f
h ν = 200 eV
as-depo
FGA 370C
IGA 370C
HVA 370C
Intensity /a.u. (Hf 4f = 1)
Binding Energy /eV
h ν = 620 eV
(c) O 1s
HfO 2 ~1nm
Intensity /a.u. (O 1s = 1)
Binding Energy /eV
h ν = 620 eV
(d) N 1s
HfO 2 ~1nm
Intensity /a.u. (N 1s = 1)
Binding Energy /eV

Figure 6.

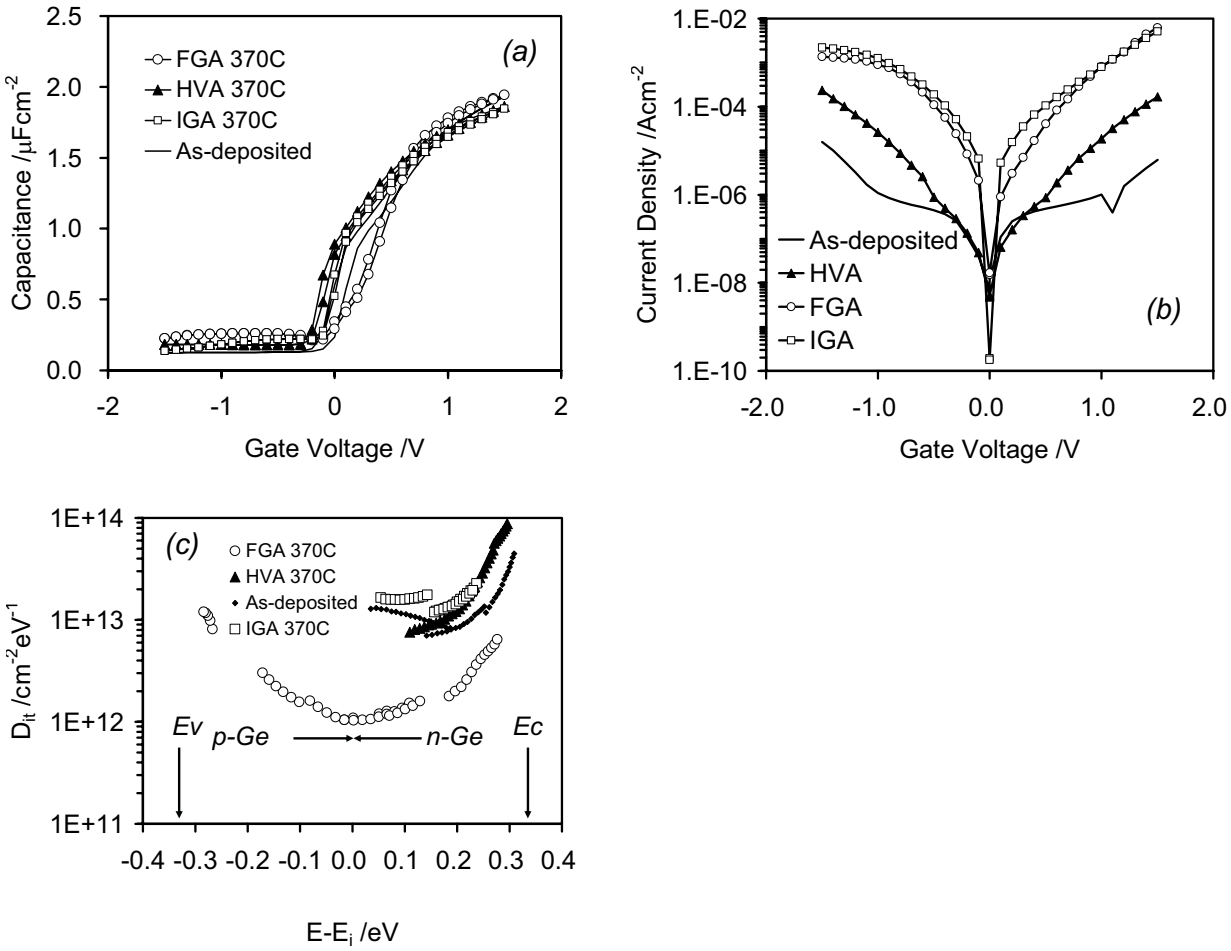
(a)
FGA 370C
HVA 370C
IGA 370C
As-deposited
Capacitance /μFcm-2
Gate Voltage /V
(b)
As-deposited
HVA
FGA
IGA
Current Density /Acm-2
Gate Voltage /V
(c)
FGA 370C
HVA 370C
As-deposited
IGA 370C
Ev
p-Ge
n-Ge
Ec
Dit /cm-2eV-1
E-Ei /eV

References

[1] C. O. Chui, S. Ramanathan, B. B. Triplett, P. C. McIntyre and K. C. Saraswat, *Elec. Dev. Lett.*, **23**, 473 (2002).

[2] Y. Fukuda, K. Kato, H. Toyota, T. Ono, Y. Nagasato and T. Ueno, *Jpn. J. Appl. Phys.*, **45**. 7351 (2006).

[3] T. Maeda, M. Nishizawa, Y. Morita and S. Takagi, *Appl. Phys. Lett.*, **90**, 072911 (2007).

[4] Y. Otani, Y. Itayama, T. Tanaka, Y. Fukuda, H. Toyota, T. Ono, M. Mitsui and K. Nakagawa, *Appl. Phys. Lett.*, **90**, 142114 (2007).

[5] S. Takagi, T. Maeda, N. Taoka, M. Nishizawa, Y. Morita, K. Ikeda, Y. Yamashita, M. Nishikawa, H. Kumagai, R. Nakane, S. Sugahara, N. Sugiyama, *Microelec. Eng.*, **84**, 2314 (2007).

[6] T. Sugawara, R. Sreenivasan and P. C. McIntyre, *J. Vac. Sci. Technol. B.,* **24**, 2442 (2006).

[7] K. Prabhakaran and T. Ogino, *Surf. Sci.,* **325**, 263 (1995).

[8] O. Vancauwenberghe, O. C. Hellman, N. Herbots and W. J. Tan, *Appl. Phys. Lett.*, **59**, 2031 (1991).

[9] C. Mui and C. B. Musgrave, *Langmuir*, **21**, 5230 (2005).

[10] T. A. Carlson and G. E. McGurie, *J. Electron Spectrosc. Relat. Phenom.* **1**, 161 (1972/1973).

[11] C. J. Powell, *NIST Inelastic-mean-free-path database Ver 1.1*, National Institute of Standards and Technology, Maryland (2000).

[12] J. E. Lowther, Phys. Rev. B, **62**, 5 (2000).

[13] C. O. Chui, K. Gopalakrishnan, P. B. Griffin, J. D. Plummer and K. C. Saraswat, *Appl. Phys. Lett.*, **83**, 3275 (2003).

[14] J.-J. Yeh, *Atomic Calculations of Photoionization Cross Sections and Asymmetry Parameters,* Gordon and Breach, Pennsylvania (1993).

[15] K. Prabhakaran, F. Maeda, Y. Watanabe and T. Ogino, *Appl. Phys. Lett.,* **76**, 2244-6 (2000).

[16] M-T. Ho, Y Wang, R.T Brewer, L.S. Wielunski, Y.J. Chabal, N. Moumen, and M. Boleslawski, *Appl. Phys. Lett.,* **87**, 133103 (2005).

[17] D. Schmeisser, R. D. Schnell, A. Bogen, F. J. Himpsel and D Rieger, *Surf. Sci.,* **172**, 455 (1986).

[18] K. Martens, B. De Jaeger, R. Bonzom, J. Van Steenbergen, M. Meuris, G. Groeseneken, and H. Maes, *Elec. Dev. Lett.*, **27**, 405(2006).

[19] D. Kuzum, T. Krishnamohan, A. J. Pethe, A. K. Okyay, Y. Oshima, Y. Sun, J. P. McVittie, P. A. Pianetta, P. C. McIntyre, and K. C. Saraswat, *Elec. Dev. Lett.*, **29**, 328 (2008).

[20] E. H. Nicollian and J. R. Brews, *MOS Physics and Technology*, Chapter 5, Wiley, New York, (1981).

[21] Y. Fukuda, T. Ueno, S. Hirono, and S. Hashimoto, *Jpn. J. Appl. Phys.*, **44**, 6981 (2005).

[22] J.R. Weber, A. Janotti, P. Rinke, and C.G.V. de Walle, *Appl. Phys. Lett.,* **91**, 142101 (2007).

[23] V. V. Afanas'ev, Y. G. Fedorenko, and A. Stesmans, *Appl. Phys. Lett.,* **87**, 032107 (2005).